nature structural & molecular biology

Spiral architecture of the Hsp104 disaggregase reveals the basis for polypeptide translocation

Adam L Yokom[1,2], Stephanie N Gates[1,2], Meredith E Jackrel[3], Korrie L Mack[3,4], Min Su[1], James Shorter[3,4] & Daniel R Southworth[1]

Hsp104, a conserved AAA+ protein disaggregase, promotes survival during cellular stress. Hsp104 remodels amyloids, thereby supporting prion propagation, and disassembles toxic oligomers associated with neurodegenerative diseases. However, a definitive structural mechanism for its disaggregase activity has remained elusive. We determined the cryo-EM structure of wild-type *Saccharomyces cerevisiae* Hsp104 in the ATP state, revealing a near-helical hexamer architecture that coordinates the mechanical power of the 12 AAA+ domains for disaggregation. An unprecedented heteromeric AAA+ interaction defines an asymmetric seam in an apparent catalytic arrangement that aligns the domains in a two-turn spiral. N-terminal domains form a broad channel entrance for substrate engagement and Hsp70 interaction. Middle-domain helices bridge adjacent protomers across the nucleotide pocket, thus explaining roles in ATP hydrolysis and protein disaggregation. Remarkably, substrate-binding pore loops line the channel in a spiral arrangement optimized for substrate transfer across the AAA+ domains, thereby establishing a continuous path for polypeptide translocation.

Heat-shock protein (Hsp) 104, found in yeast, is a member of the Hsp100 class of molecular chaperones, which contain highly conserved ATPase domains associated with diverse cellular activities (AAA+) and have essential roles in thermotolerance and protein quality control[1–3]. Hsp104 and its bacterial homolog, ClpB, form large hexameric ring structures that cooperate with the Hsp70 system in unfolding and rescuing aggregated protein states via active translocation of polypeptide substrates through a central channel[4–6]. In addition to solubilizing stress-induced disordered aggregates[5,7], Hsp104 recognizes and remodels cross-β structures of amyloid fibrils, such as those found in Sup35 prions, thereby enabling Hsp104 to control prion inheritance in yeast[8–10]. This function in prion disaggregation is enhanced in Hsp104 compared with ClpB, and studies have identified potentiated Hsp104 variants that decrease the toxicity of proteins, including TDP-43, FUS and α-synuclein, that have been linked to neurodegenerative diseases[11–13]. Despite its fundamental roles in protein quality control and its promising therapeutic activity in rescuing amyloidogenic states[14], how Hsp104 and its family members function as powerful molecular motors that solubilize proteins is not fully understood.

Hsp104 and ClpB contain a mobile N-terminal domain (NTD), which has been implicated in substrate engagement[15,16]; two evolutionarily distinct AAA+ nucleotide-binding domains (NBD1 and NBD2), which bind substrates and power translocation; and a middle domain (MD), which is required for disaggregation and interaction with Hsp70 (refs. 17–21 and **Fig. 1a**). Hsp104 also contains a C-terminal domain (CTD) that is not found in ClpB and is required for hexamerization[22]. The crystal structure of ClpB[23] from a thermophilic eubacterium (*Thermus thermophilus*) identifies the conserved type II AAA-domain architecture wherein the NBDs comprise large and small subdomains that form the ATP-binding pocket and contain the respective Walker A and B motifs and 'sensor' residues required for ATP hydrolysis. The MD, located within the small subdomain of NBD1, forms an ~85-Å-long, flexible coiled coil that has been proposed to adopt a number of conformations in the hexamer during the hydrolysis cycle[23–27].

Polypeptide translocation between NBD1 and NBD2 is controlled via allosterically driven ATP-hydrolysis events[28,29], and, for Hsp104, cooperativity among protomers is required for disaggregation of highly stable amyloids[30]. Substrate binding is favored in the ATP-bound state[31] and involves direct interaction with highly conserved tyrosine residues in flexible NBD 'pore loops'[5,6,32] that have been proposed to line the axial channel and operate by hydrolysis-driven substrate-handoff cycles. How this occurs across the 100-Å-long channel and between the two distinct AAA+ domains remains unknown. A number of cryo-EM models of Hsp104 mutants[25,29,33] and ClpB[23,24] at modest resolutions between 11 and 20 Å have been described and suggest various structural arrangements but generally show a symmetric hexamer with three distinct rings comprising the NTD, NBD1 and NBD2. Structural studies have also identified different nucleotide states that involve changes in the pore diameter and conformation of the domains[24,27,29]. However, the oligomeric state

[1]Department of Biological Chemistry, Life Sciences Institute, University of Michigan, Ann Arbor, Michigan, USA. [2]Graduate Program in Chemical Biology, Life Sciences Institute, University of Michigan, Ann Arbor, Michigan, USA. [3]Department of Biochemistry and Biophysics, Perelman School of Medicine, University of Pennsylvania, Philadelphia, Pennsylvania, USA. [4]Biochemistry and Molecular Biophysics Graduate Group, Perelman School of Medicine, University of Pennsylvania, Philadelphia, Pennsylvania, USA. Correspondence should be addressed to D.R.S. (dsouth@umich.edu).

Received 16 May; accepted 11 July; published online 1 August 2016; doi:10.1038/nsmb.3277

is dynamic, requiring the presence of nucleotide for stability[34], and the protomers exchange rapidly during the hydrolysis cycle[30,35,36]; consequently, the high-resolution architecture of the active hexameric complex has remained out of reach.

Here we set out to elucidate the structural mechanism of the Hsp104 disaggregase. We determined the cryo-EM structure of wild-type (WT) Hsp104 from yeast (*S. cerevisiae*) bound to the nonhydrolyzable ATP analog AMP-PNP, at 5.6-Å resolution. The structure reveals a helical-like arrangement involving a 10-Å rise between protomers that results in a seam at which the first protomer is offset by more than 40 Å from the sixth protomer. This offset brings NBD1 from one protomer into contact with NBD2 in the adjacent protomer, and a heteromeric AAA+ interaction is formed at the seam. Well-defined density corresponding to the conserved tyrosine pore loops presents a spiral of substrate-binding surfaces along the axial channel. Remarkably, the protomer offset optimally positions the NBD1 and NBD2 pore loops at the seam, thus allowing for coordinated transfer of substrates across the AAA+ domains.

RESULTS

The Hsp104 hexamer adopts an asymmetric spiral architecture

We determined the cryo-EM structure of the intact WT Hsp104 complex in the presence of AMP-PNP, to mimic the substrate-binding ATP state[8]. Purified Hsp104 was functionally active in ATPase and disaggregase assays (**Supplementary Fig. 1a**,**b**). The cryo-EM images of Hsp104–AMP-PNP show homogeneous oligomeric complexes (**Supplementary Fig. 1c**), and reference-free 2D classification reveals a variety of distinct views with well-resolved structural features (**Supplementary Fig. 1d**). These 2D averages reveal clear top-view ring shapes and side views that show a striking asymmetry and unique protomer arrangement different from that previously described[25,29] (**Fig. 1b**). We achieved the final cryo-EM reconstruction after 3D refinement with no imposed symmetry, at resolutions of 6.5 Å and 5.6 Å for the unmasked and masked maps, respectively (**Supplementary Fig. 1e**). The final map comprises 85% of the single-particle data after sorting by 2D classification. The 3D classification identified no additional conformations or oligomeric states (data not shown); thus, the final map represents the predominant form of Hsp104 in the data set. The angular distribution of the particles shows several preferred orientations (**Supplementary Fig. 1f**), and 2D projections of the 3D map match the reference-free averages, thereby confirming the overall asymmetric architecture (**Supplementary Fig. 1g**).

The 3D reconstruction reveals that Hsp104–AMP-PNP is a ring-shaped hexamer with three distinct domain layers that correspond to the NTD, NBD1 MD and NBD2, a result consistent with those from other studies[25,29,33] (**Fig. 1c** and **Supplementary Video 1**). In striking contrast to previous models, the protomers are arranged in a helical spiral, and the NBD rings connect, forming a distinct asymmetric seam. The NBD1 and NBD2 show the highest-resolution density, at approximately 5 Å, whereas the NTDs as well as regions at the hexamer seam are more flexible, at ~6- to 7-Å resolution (**Supplementary Fig. 1h**). The density for the MD coiled coil is partly resolved on one face of the hexamer, where it wraps around the outside of the hexamer adjacent to the NBD1s (**Fig. 1c**). The central channel is approximately 25–30 Å in diameter but opens into a wide cleft at the hexamer seam, owing to the spiral offset of the adjacent protomers.

We used the crystal structure of *T. thermophilus* ClpB[23] (PDB 1QVR), a protein with ~45% sequence identity with Hsp104, for initial fitting and determination of a homology model for Hsp104. Helices are designated as they are in the ClpB structure (**Supplementary Fig. 2a**). We docked the reconstruction by rigid-body fitting of the domains and then performed flexible fitting to achieve an atomic model with the highest correlation to the map, at 0.92. The protomers are designated 1 through 6, such that protomer 1 (P1) is in the highest position in the side-view orientation, and the numbers proceed counterclockwise as viewed from the NTD face (**Fig. 2a**,**b**). The NBDs fit well, with a cross-correlation value of 0.94, and identify the conserved AAA+ subdomain architecture with α-helical and β-sheet regions that are well resolved for each of the protomers (**Fig. 2c** and **Supplementary Video 2**). Difference-map analysis between the final map and a nucleotide-free model indicated that nucleotide is present in the majority of the NBDs, and we observed clear density in nine sites, reduced density in two sites, indicating partial occupancy or flexibility, and no density at one site (**Supplementary Fig. 2b**). The NBD1s show a canonical AAA+ arrangement, including expected positions for the Walker A (K218), Walker B (E285) and sensor 1 (T317) residues. Putative arginine-finger residues R334 and R333 (ref. 25) are within 7 and 10 Å, respectively, of the nucleotide pocket of the adjacent protomer, thus indicating a catalytically active arrangement. The NBD2s are similarly well defined, showing conserved interprotomer interactions and positions for the Walker A (K620), Walker B (E687), sensor 1 (N728) and sensor 2 (R826) residues,

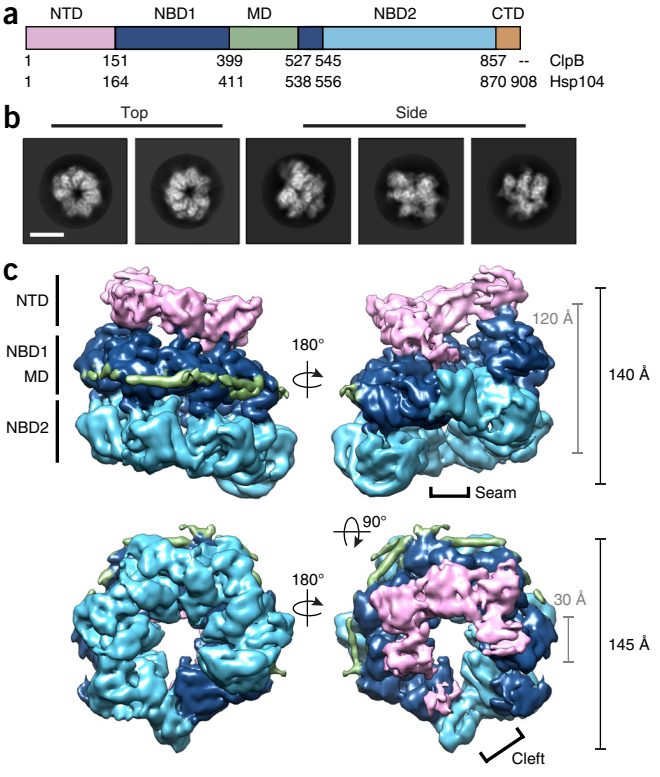

Figure 1 Spiral architecture and three-tiered domain arrangement of the Hsp104 hexamer complex, determined by cryo-EM. (**a**) Schematic showing individual domains and corresponding residue numbers for *T. thermophilus* ClpB and *S. cerevisiae* Hsp104. (**b**) Reference-free 2D cryo-EM class averages of Hsp104 showing top and side views representative of 190 similar averages including 300 or more particles each. Scale bar, 100 Å. (**c**) Views of the final sharpened 3D density map (4σ) of Hsp104, showing a spiral three-tier architecture. The domains are colored as in **a**, on the basis of the atomic model. Approximate dimensions of the channel (gray) and exterior (black) are shown, and the hexamer seam and channel cleft are indicated.

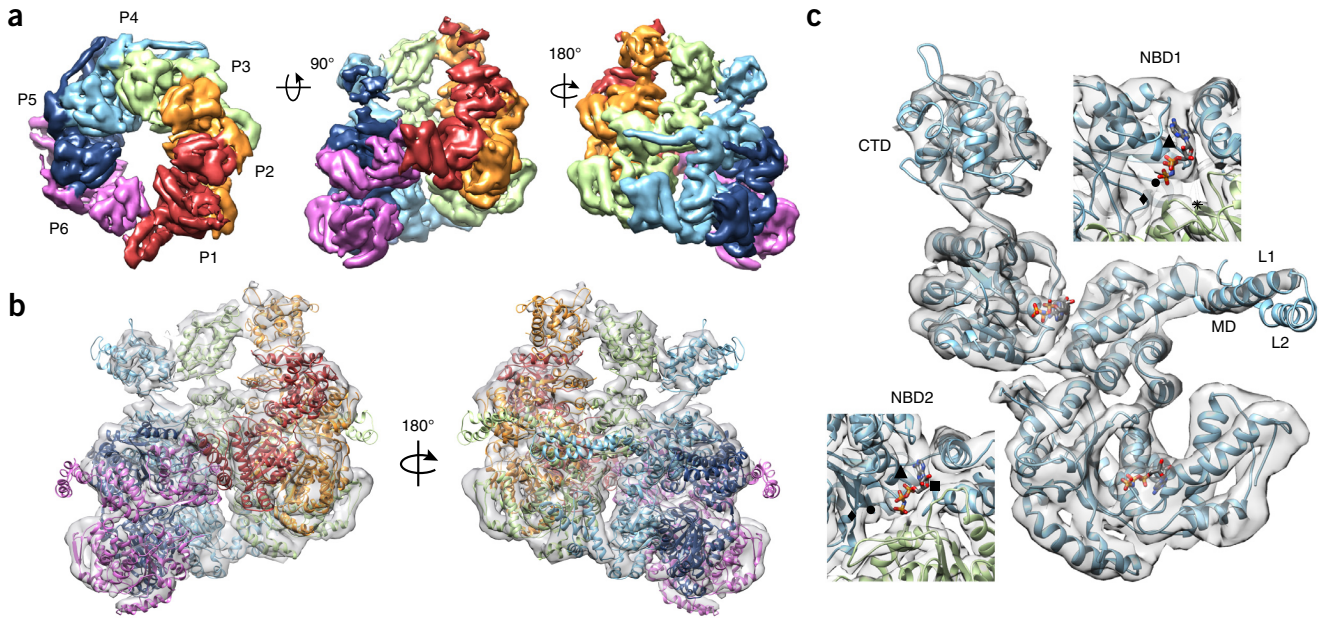

Figure 2 Protomer arrangement and molecular model of Hsp104. (**a**) Top view, showing NBD1 density and protomer labels, and side views of the sharpened map (5σ). Each protomer is colored according to the molecular model. (**b**) Side views of the Hsp104 hexamer molecular model, determined by flexible fitting of the homology model based on the ClpB structure[23] (PDB 1QVR). (**c**) Molecular model of a segmented protomer (P4), showing bound nucleotides and well-resolved density for the NBD1 and NBD2 AAA+ domains. Enlarged views of the nucleotide pockets are shown with indicated positions for Walker A (triangle), Walker B (diamond), sensor 1 (circle), sensor 2 (square) and arginine-finger (asterisk) residues.

and the proposed arginine finger (R765)[37] is near the nucleotide pocket, at less than 10 Å, according to our model (**Fig. 2c**). Protomers P1 and P6, which make up the unusual hexamer seam, are in a different conformation and are discussed in further detail below.

Density corresponding to the MD coiled coil, which is partly resolved for P3–P6, was docked with residues 409–467, comprising helix L1 and part of helix L2, which connect to the NBD1 large subdomain (**Fig. 2c**). Density for the C-terminal-half of the extended

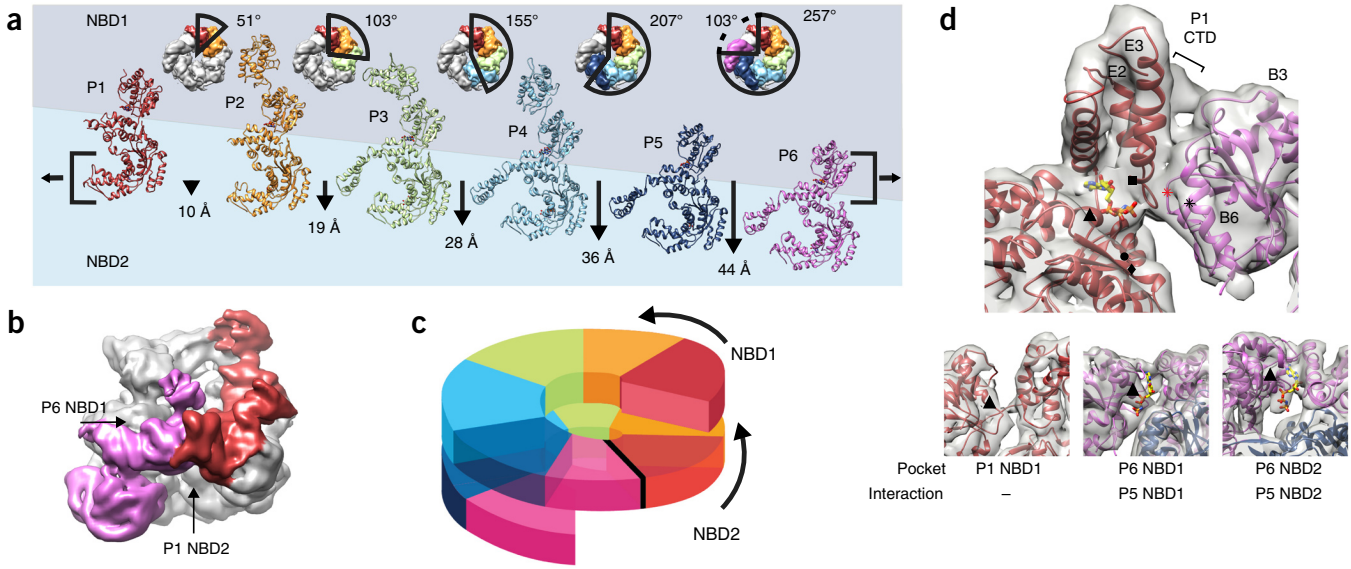

Figure 3 Basis for the protomer spiral and NBD1-NBD2 AAA+ interaction at the hexamer seam. (**a**) Protomer positions shown in top views and individually unrolled from the hexamer, with the indicated rotation and translation shift relative to P1. Brackets indicate alignment of NBD1 and NBD2 AAA+ domains for P6 and P1, respectively. (**b**) Low-pass-filtered map colored for P1 (red) and P6 (magenta), highlighting the P6 NBD1–P1 NBD2 interaction. (**c**) Cartoon model showing that the NBD1 and NBD2 AAA+ domains connect and form a two-turn spiral. (**d**) Expanded view of the model and map showing the NBD1-NBD2 interaction from inside the channel. Interface regions are indicated: B3 and B6 helices (NBD1 large subdomain), E2 and E3 helices (NBD2 small subdomain) and the P1 CTD. Positions for the Walker A (triangle), Walker B (diamond), sensor 1 (circle), sensor 2 (square) and putative arginine-finger residues R333 and R334 (asterisk) and R307 (red asterisk) are indicated. Nucleotide pockets for the P1 NBD1, P6 NBD1 and P6 NBD2 are shown with Walker A residues (triangle) indicated. Nucleotide is shown for sites with density observed in the pocket.

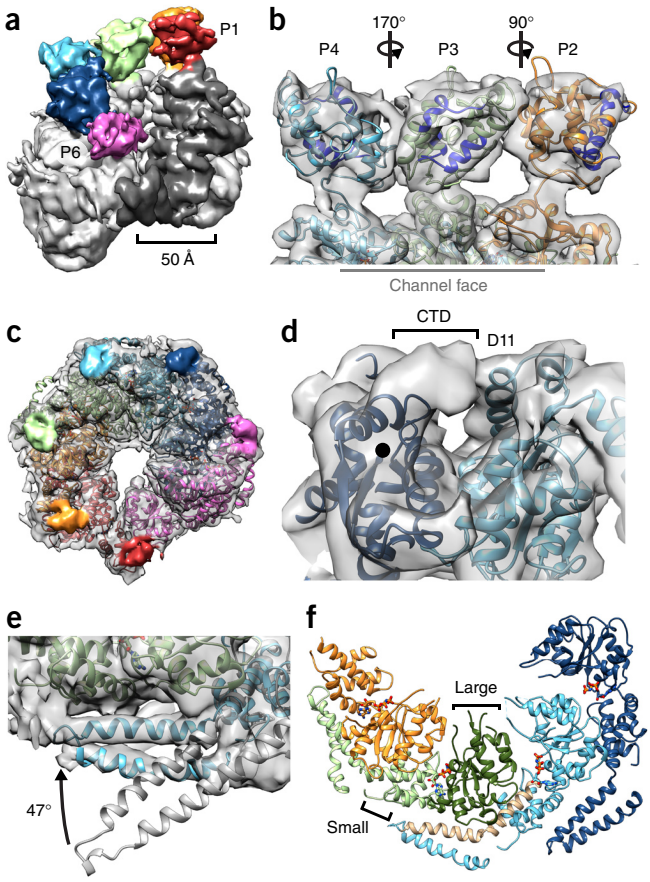

Figure 4 Distinct arrangements of the NTD, MD and CTD in the hexamer. (**a**) 3D map in a tilted orientation showing the NTDs, colored by protomer, interacting around the channel entrance and the 50-Å-wide cleft defined by the P1 and P6 NTDs and P1 AAA+ (dark gray). (**b**) Enlarged view of the modeled P2–P4 NTDs, showing different orientations around the NBD1 connecting linker. Rotations are relative to P3, and hydrophobic substrate–binding sites[15] are indicated (blue). (**c**) View of the NBD2 channel exit face of the hexamer with the density corresponding to the CTDs colored by protomer. (**d**) Enlarged view of the P5 CTD density extending from the NBD2 C terminus (circle) and interacting with P4 NBD2, at adjacent helix D11. (**e**) Comparison between the MD L1 and L2 orientation based on the docked ClpB structure[23] (gray) and Hsp104 model showing 47° rotation around C3–L1 connecting residues (409–410) to fit the density. (**f**) View of the NBD1 MD interactions for P2–P5, showing helices C3–L1 (brown) bridging across the large (dark green) and small (light green) subdomains of the adjacent protomer.

85-Å helix L2 as well as helix L3 and helix L4, a region including Hsp70-interaction sites[18], was not clearly identifiable, thus indicating that this portion of the MD remains flexible. The NTDs form globular lobes of density that interact, following the helical arrangement of the NBDs, and form a broad entrance to the channel (**Figs. 1c** and **2a**). Despite the NTD's flexibility, the good definition of the NTD NBD1 linkers enabled unambiguous connection to the corresponding protomer. We were able to model NTD structures for protomers P2–P4 (**Fig. 2b**), which exhibit the best-resolved features, and the cross-correlation of the fit was 0.91. Further details of the MD and NTD conformations are discussed below.

Heteromeric NBD1-NBD2 interaction defines the hexamer seam

The most striking structural feature of the Hsp104 hexamer is the helical-like arrangement of the protomers. Canonical AAA+ interactions are generally maintained around the hexamer; however each protomer is tilted slightly, thus resulting in an approximate seven-fold helical symmetry. From P1 to P6, the protomers each rise nearly 10 Å and rotate 53°, on average (**Fig. 3a**). The conformations and position of the individual protomers vary around the hexamer, thus indicating that the complex is indeed asymmetric (**Supplementary Fig. 3a**). When the NBD1s are superimposed, continuous conformational changes are apparent from P1 to P6 (**Supplementary Fig. 3b**), and the greatest protomer differences occur between P1 and P6 at the hexamer seam (**Supplementary Fig. 3c**). The conformational changes primarily involve rotations of the NBD1 and NBD2 small subdomains, which move inward relative to the channel axis by approximately 10° and 20°, respectively, thus resulting in a more compact P1 protomer compared with P6 (**Supplementary Fig. 3c**).

The helical shift of the protomers results in a 44 Å-offset between P1 and P6, yet these protomers interact together, covering a 100° rotation around the channel axis and completing the hexamer ring (**Fig. 3b**). Remarkably, this large offset positions the P6 NBD1 adjacent to the P1 NBD2 and results in an NBD1-NBD2 interaction that connects the AAA+ domains in a two-turn spiral (**Fig. 3c**). The density, although at a slightly lower resolution compared with that of the other protomers, is well defined in this region and reveals interactions mediated by the B3 and B6 connecting loops from the P6 NBD1 and helices E2 and E3 from the P1 NBD2 (**Fig. 3d**). Density corresponding to the P1 CTD also contacts the P6 NBD1 toward the outside of the channel, thus potentially stabilizing the interaction.

Despite the unusual NBD1-NBD2 interaction, density corresponding to bound nucleotide is present for the P1 NBD2 and indicates a potentially active catalytic site (**Fig. 3d** and **Supplementary Fig. 2b**). Although the interprotomer AAA+ interaction is different from interactions at the more canonical interfaces at the other sites, putative arginine-finger residues R334 and R333 in the P6 NBD1 are localized approximately 10–12 Å away from the P1 NBD2 nucleotide pocket. Interestingly, another highly conserved arginine residue, R307 in P6, is within 5 Å of the P1 NBD2 pocket. Thus, either a small conformational change that repositions R334 or R333, or activation by R307 could support ATP hydrolysis. In contrast, we did not observe density in the P1 NBD1 pocket, a result indicating that nucleotide is not present (**Fig. 3d**). However, because of the protomer offset, the P1 NBD1 is not supported by an adjacent AAA+ domain from P6, and hence the nucleotide pocket is likely to be destabilized and inactive. Despite the apparent canonical orientation of the adjacent P5 NBD1, density in the P6 NBD1 pocket appears weak relative to that for the other protomers, thus indicating partial occupancy or flexibility. Finally, we observed nucleotide density for the P6 NBD2; this site is supported by the adjacent P5 NBD2, which is in an arrangement similar to those of the other protomers. Overall, comparison of the AAA+ domains for protomers 1 and 6 revealed a mix of nucleotide states and an asymmetric structural organization with interactions that are distinct from those in the rest of the hexamer and potentially support unique functions during disaggregation.

Arrangement of the MD and NTD highlights critical functions

The conserved NTDs bind hydrophobic regions of substrates and have been proposed to direct polypeptides to the NBD pore loops as well as enhance cooperative substrate binding required for amyloid disaggregation[15,27]. In our Hsp104 map, the P1–P5 NTDs surround the axial channel, forming a C-shaped entrance approximately 35 Å in diameter (**Fig. 4a**). The opening widens substantially to approximately 50 Å, moving toward the P6 NTD at the hexamer seam and creating

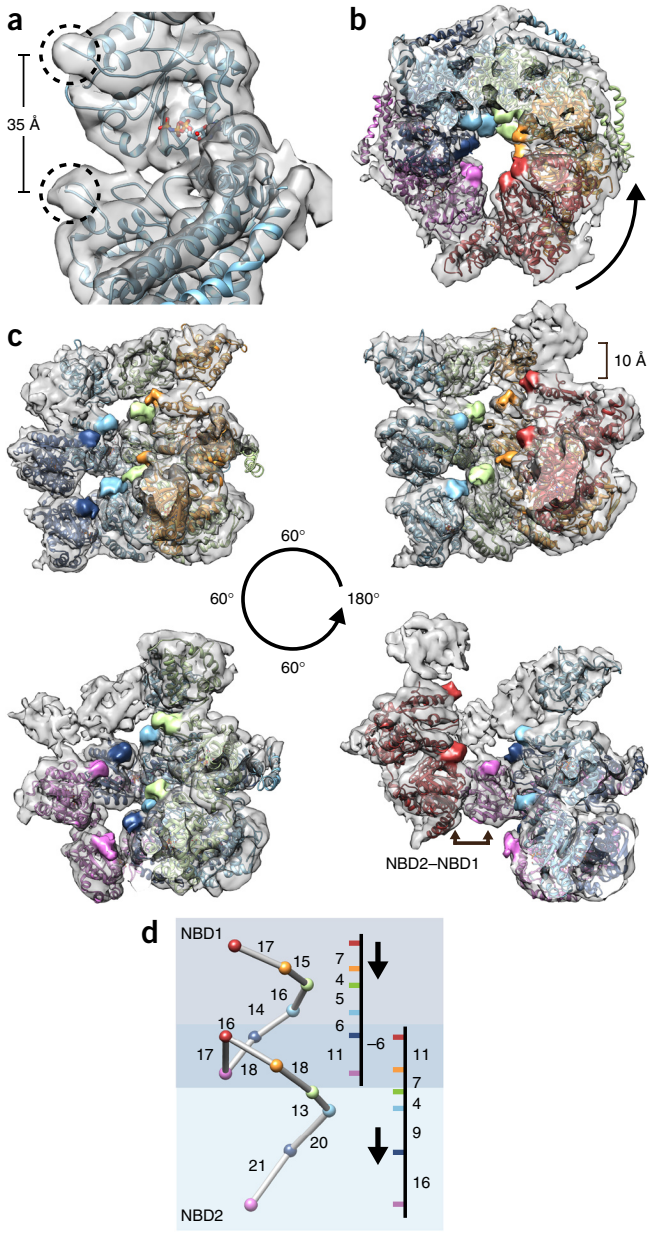

Figure 5 Two-turn spiral arrangement of the substrate-binding tyrosine pore loops around the channel. (**a**) Density corresponding to the tyrosine pore loops (circled) for NBD1 and NBD2 is shown for P4. (**b**) View down the channel from the NBD1 face. The pore-loop densities are colored according to protomer. The arrow indicates a counterclockwise shift between adjacent protomers moving down the channel. (**c**) Rotated views from inside channel, showing the two-turn spiral organization of the pore loops and putative P6 NBD1 to P1 NBD2 substrate-transfer site. (**d**) Distances between the pore loops and the corresponding movement down the channel axis are shown in angstroms.

a large cleft that opens along the side of the hexamer. Although the P6 NTD is more flexible and less well resolved, interactions between the adjacent P5 NTD as well as an unusual interaction with P1 NBD2 are visible when viewed at a reduced threshold for the density (**Fig. 4a**). Because of the NTD separation, the P1 NBD1 largely defines an equatorial channel entrance. On the basis of the arrangement in the other protomers, the P1 MD would extend across the cleft toward the P6 NTD; however, the density was not sufficiently resolved for localization. The molecular models of the P2–P4 NTDs reveal that only the P3 NTD is positioned with its hydrophobic substrate–binding cleft[15] facing toward the channel, while the P2 and P4 NTDs each adopt different orientations (**Fig. 4b**). Thus, whereas the NTDs interact and form a defined ring at the channel entrance, the interfaces are variable and multiple conformations are adopted around the hexamer, thus potentially enabling binding to heterogeneous protein-aggregate surfaces.

In contrast, the channel exit on the opposite face of the hexamer is largely defined by the NBD2; however, we observed an additional lobe of density in all protomers, which we predict corresponds to the 38-residue CTD (**Fig. 4c**). The density emerges from the NBD2 C-terminal site identified on the basis of ClpB and extends and forms a defined bridge connection to the adjacent protomer by contacting helix D11 in NBD2 (**Fig. 4d**). The interaction probably stabilizes the hexamer, as suggested by previous studies[22], and the CTD position around the channel exit also explains previously proposed functions in cochaperone binding[38] and therefore might serve as a docking point for substrate handoff to downstream chaperone systems.

On the basis of the fit of the MD L1 and L2 helices for P3–P6, the MD is rotated 47° compared with its position in the crystal structure and directly contacts NBD1 of the adjacent protomer (**Fig. 4e**). L1 and L2 are positioned alongside the clockwise neighbor and, together with helix C3, form a 60-Å-long strap across the small and large AAA+ subdomains (**Fig. 4f**). The interaction is with the opposite protomer that makes up the canonical AAA+ interface, such that each NBD1 is supported by the MD of one neighbor and the large AAA+ subdomain of the other neighbor. Density in this region is well defined for helix L1, which contacts helix C1, the C1–C2 connecting loop and part of helix B3 in the neighboring protomer. The interaction appears to involve conserved residues R419, E427 and D434, which have been previously identified to be critical for function[25,39,40]. We found that these residues are positioned to interact with E190, R353 and R366, respectively, in the adjacent NBD1 and may form stabilizing salt-bridge interactions (**Supplementary Fig. 4**).

Spiral staircase of pore loops defines the substrate path

Each NBD contains flexible loop regions that contain the conserved tyrosine residues (Y257 for NBD1 and Y662 in NBD2) that bind polypeptide substrates and are required for disaggregation[5,6,32,41]. However, these pore loops are not resolved in the ClpB structure[23], and how polypeptides could be actively transferred from protomer to protomer and across the two AAA+ domains has been unclear. By flexible fitting, we were able to model pore-loop residues for NBD1 (excluding residues 253–258) and NBD2 (excluding residues 660–666) within large lobes of density identified in the channel (**Fig. 5a**). The NBD1 and NBD2 pore loops are separated by 35–40 Å, depending on the protomer, and they project toward the channel axis in a staggered counterclockwise arrangement, as viewed down the N-terminal channel entrance (**Fig. 5b**).

As viewed from inside the channel, the NBD1 and NBD2 pore loops form a two-turn spiral staircase (**Fig. 5c** and **Supplementary Video 3**). The P1 NBD1 pore loop is nearest to the NTD channel cleft, and each subsequent loop is 15–20 Å away, down the channel (**Fig. 5d**). The distances between the pore loops vary, such that there is greater separation near the hexamer seam, particularly between P5 and P6, which are separated by 20 Å, thus reflecting conformational differences in the protomers. Notably, we observed additional lobes of density beneath the NBD1 pore loops, corresponding to residues 288–298, which may serve as additional substrate-binding surfaces via electrostatic interactions (**Supplementary Fig. 5**).

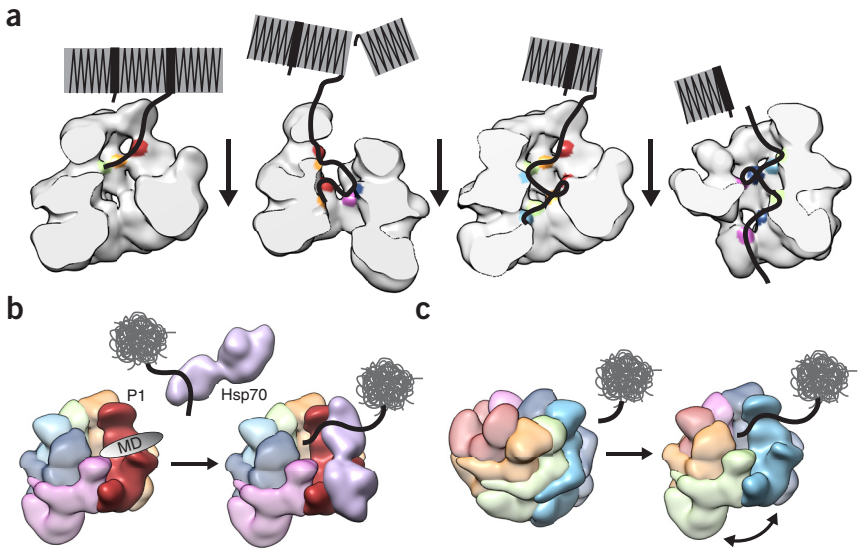

Figure 6 Models for cooperative disaggregation and substrate engagement by Hsp104. (**a**) Disaggregation of structured amyloids is depicted, showing cooperativity between protomers facilitated by the spiral architecture, which enables ordered polypeptide transfer across short distances and between the two AAA+ domains. (**b**) The hexamer seam and cleft between P1 and P6 presents a channel entrance and an optimal configuration for substrate binding and Hsp70 interaction via the P1 MD. (**c**) Depiction of protomer rearrangements, triggered by substrate binding, that could result in formation of the hexamer seam at the site of engagement and facilitate polypeptide translocation into the channel.

Indeed, this corresponding region in ClpA has been shown to interact directly with substrate[42]. The NBD1 loops are positioned approximately 10 Å away from the respective NTDs for each protomer; thus, substrates could be transferred to the NBD at multiple sites around the channel. Remarkably, the heteromeric NBD1-NBD2 interaction at the hexamer seam positions the respective pore loops 17 Å apart, a distance similar to the others, thus revealing a contiguous substrate-transfer pathway between the AAA+ domains.

DISCUSSION

The lack of a definitive structure of the active Hsp104 hexamer has hindered understanding of how these conserved AAA+ complexes function as disaggregase machines. Previous cryo-EM structures have been critical in revealing the overall hexameric three-tier architecture[24,25,29,33] but are limited in resolution, probably because of available cryo-EM technology, heterogeneity and imposed symmetry. By using the latest cryo-EM technical advances and acquiring a substantial single-particle data set for exhaustive classification and alignment, we achieved a structure of Hsp104 that provides the first evidence, to our knowledge, that the hexamer adopts an asymmetric near-helical architecture that connects the AAA+ domains around the channel. This unprecedented spiral arrangement provides a structural mechanism that explains how cooperative interactions between the protomers and across the AAA+ domains by Hsp104 might drive processive polypeptide translocation[27,28,30].

The left-handed spiral of the Hsp104 hexamer establishes a substrate-binding path that appears to be optimally organized for transfer from protomer to protomer counterclockwise around the channel; consequently, directional polypeptide movement from the NTD entrance to the NBD2 exit can be achieved (**Fig. 6a**). The NBD1-NBD2 interaction aligns the pore loops, thereby facilitating substrate transfer across the AAA+ domains and enabling two or more cycles of interaction per protomer. This mechanism is likely to be necessary for substrates such as structured amyloids, which are dependent on high protomer cooperativity and action from both AAA+ domains[30]. Polypeptide threading may occur more stochastically or involve a subset of protomers, such as for disordered, unstructured aggregates, as proposed in previous studies[16,30]. Nonetheless, the staircase arrangement of binding surfaces explains how Hsp104 can cooperatively use both AAA+ domains for more powerful unfolding. This mechanism is a remarkable extension of unidirectional threading models based on the asymmetric architecture of ClpX[3,43], which exhibits a staggered arrangement of pore loops around its single AAA+ ring. Although the translocation step size is unknown for Hsp104, it is expected to be less than 30 Å, on the basis of measurements of ClpB[44], ClpX[45,46] and ClpA[47]. The 15- to 20-Å distance that we identified between pore loops is consistent with this prediction and suggests that polypeptide translocation occurs through short stepwise transfer events. Given the homology, we expect that related ClpB and other type II Hsp100 family members may adopt a spiral architecture similar to that of Hsp104. Indeed, the ClpA[48] and ClpB[23] protomers each form unique left-handed spirals in the crystal. However, both display mechanistic differences: ClpA functions in conjunction with a bound ClpP protease[49], whereas ClpB has been proposed to operate via nonprocessive translocation events[30,44]; thus, these complexes may adopt different hexamer arrangements in solution.

The asymmetric seam and protomer offset present a unique architecture that is likely to be functionally significant. The P1 NTD and NBD1 substrate-binding surfaces are at the topmost axial position and are accessible because of the 50-Å-wide cleft formed by separation of the P1 and P6 NTDs (**Fig. 4a**). Thus, initial substrate engagement may involve preferential interactions with this protomer and may be followed by sequential downstream transfer to P2–P6. Furthermore, the cleft at the hexamer seam opens directly to the P1 NTD and MD, and presents an optimal site for Hsp70 to interact and transfer substrates to the channel (**Fig. 6b**). The interface at the hexamer seam may also play critical roles in the functional plasticity of Hsp104 (ref. 27) by facilitating recognition and engagement of different aggregate structures. Finally, given the known nucleotide-dependent dynamics of the hexamer[36], a compelling mechanism is that reorganization of the protomer offset is triggered by substrate binding, Hsp70 interaction or ATP hydrolysis and consequently facilitates translocation (**Fig. 6c**).

A number of different MD arrangements have been proposed on the basis of previous low-resolution models[23–26,33]. Our structure reveals the clearest view to date of the MD conformation in the ATP state and identifies bridging interactions, occurring between L1 and L2 and the small and large subdomains of the adjacent protomer, that potentially stabilize the nucleotide pocket for hydrolysis. The observed potential salt-bridge interactions involving R419, E427 and D434 (**Fig. 4f** and **Supplementary Fig. 4**) are consistent with the contact between L1 and the adjacent NBD1 identified through fluorescence resonance energy transfer experiments with ClpB[40], and the functional deficiency of Hsp104 R419M demonstrated in mutagenesis studies[25]. Hsp70 binds the opposite end of the MD coiled

coil at helices L2 and L3 and consequently delivers substrates and promotes disaggregation[18,20,50]. The MD L1-L2 interactions may serve as control elements for allosteric activation by Hsp70 during substrate delivery[19,40]. Indeed, mutations in L1 eliminate collaboration with Hsp70 (ref. 21) and allow disaggregation to occur independently of Hsp70 and Hsp40 (ref. 12).

In addition to our results here, a number of recent cryo-EM structures of AAA+ complexes, notably including the Pex1–Pex6 (ref. 51) and NSF[52] double AAA+ ring complexes, have identified asymmetric states. Together such studies are beginning to reveal that AAA+ proteins generally operate via large asymmetries in their protomer organization and hydrolysis mechanisms[43]. As compared with these related complexes, Hsp104 is unique in that it adopts a two-turn spiral involving interaction between the different AAA+ (NBD1 and NBD2) domains. Both Pex1–Pex6 and NSF complexes exhibit a planar, symmetric NBD1 ring that is flexibly connected to an asymmetric NBD2 ring. In Hsp104, the orientation between the two AAA+ domains within a protomer is relatively consistent around the ring, except for the hexamer seam. At this position, conformational differences between P6 and P1, including a 20° rotation of NBD2 relative to NBD1, enable the NBD1-NBD2 interaction and a closed hexamer ring despite the substantial 100° rotation around the channel axis (compared with ~50° for the other protomers) (**Fig. 3a**). In addition, we identified density corresponding to a bound nucleotide for 9 out of 12 ATP-binding sites, whereas two sites show partial occupancy, and one site is empty. This finding is consistent with previous estimates of a nucleotide occupancy of 8–12 nucleotides for ClpB hexamers[26,53], and it supports an asymmetric hydrolysis mechanism. Intriguingly, the NBD1s overall have a lower nucleotide occupancy than the NBD2s, which are completely bound. Similarly, kinetic studies have determined that the NBD1, compared with NBD2, has a lower ATP affinity but much higher catalytic activity[28], a result supporting distinct functions during disaggregation. Nonetheless, with this overall high nucleotide occupancy together with the spiral architecture, the power of the two AAA+ domains appears to be uniquely coupled for Hsp104 compared with other AAA+ complexes and is perhaps reflective of the mechanical force required for disaggregation. Additional studies will be critical in elucidating conformational changes associated with ATP-hydrolysis-dependent translocation events, to determine the mechanical changes that drive disaggregation.

METHODS

Methods and any associated references are available in the online version of the paper.

Accession codes. The cryo-EM density map (EMD-8267) has been deposited in the Electron Microscopy Data Bank, and the molecular model (PDB 5KNE) has been deposited in the Protein Data Bank.

Note: Any Supplementary Information and Source Data files are available in the online version of the paper.

ACKNOWLEDGMENTS

The authors thank J. Smith, Z. March, M. DeSantis, E. Sweeny and J. Lin for reading and discussing the manuscript; S. King for help with figures; and A. Tariq for technical assistance with Hsp104 purification. This work was supported by National Institutes of Health (NIH) grant R01GM099836 (to J.S.). A.L.Y. is supported by an American Heart Association Predoctoral fellowship; M.E.J. is supported by a Target ALS Springboard Fellowship. K.L.M. is supported by an NSF Graduate Research Fellowship (DGE-1321851). J.S. is supported by a Muscular Dystrophy Association Research Award (MDA277268), the Life Extension Foundation, the Packard Center for ALS Research at Johns Hopkins University, and Target ALS. D.R.S. is supported by NIH grants R01GM109896, R01GM077430 and R01GM110001A.

AUTHOR CONTRIBUTIONS

A.L.Y. designed experiments, performed cryo-EM sample preparation, data collection and analysis, and wrote the manuscript; S.N.G. performed cryo-EM data collection and analysis; M.E.J. purified proteins, performed biochemical analysis and edited the manuscript; K.L.M. performed biochemical analysis; M.S. supervised cryo-EM data collection; J.S. designed experiments and edited the manuscript; D.R.S. designed and supervised the study and edited the manuscript.

COMPETING FINANCIAL INTERESTS

The authors declare no competing financial interests.

1. Sanchez, Y. & Lindquist, S.L. HSP104 required for induced thermotolerance. *Science* **248**, 1112–1115 (1990).
2. Parsell, D.A., Kowal, A.S., Singer, M.A. & Lindquist, S. Protein disaggregation mediated by heat-shock protein Hsp104. *Nature* **372**, 475–478 (1994).
3. Mogk, A., Kummer, E. & Bukau, B. Cooperation of Hsp70 and Hsp100 chaperone machines in protein disaggregation. *Front. Mol. Biosci.* **2**, 22 (2015).
4. Glover, J.R. & Lindquist, S. Hsp104, Hsp70, and Hsp40: a novel chaperone system that rescues previously aggregated proteins. *Cell* **94**, 73–82 (1998).
5. Weibezahn, J. *et al.* Thermotolerance requires refolding of aggregated proteins by substrate translocation through the central pore of ClpB. *Cell* **119**, 653–665 (2004).
6. Lum, R., Tkach, J.M., Vierling, E. & Glover, J.R. Evidence for an unfolding/threading mechanism for protein disaggregation by *Saccharomyces cerevisiae* Hsp104. *J. Biol. Chem.* **279**, 29139–29146 (2004).
7. Motohashi, K., Watanabe, Y., Yohda, M. & Yoshida, M. Heat-inactivated proteins are rescued by the DnaK.J-GrpE set and ClpB chaperones. *Proc. Natl. Acad. Sci. USA* **96**, 7184–7189 (1999).
8. Shorter, J. & Lindquist, S. Hsp104 catalyzes formation and elimination of self-replicating Sup35 prion conformers. *Science* **304**, 1793–1797 (2004).
9. Chernoff, Y.O., Lindquist, S.L., Ono, B., Inge-Vechtomov, S.G. & Liebman, S.W. Role of the chaperone protein Hsp104 in propagation of the yeast prion-like factor [psi+]. *Science* **268**, 880–884 (1995).
10. Moriyama, H., Edskes, H.K. & Wickner, R.B. [URE3] prion propagation in *Saccharomyces cerevisiae*: requirement for chaperone Hsp104 and curing by overexpressed chaperone Ydj1p. *Mol. Cell. Biol.* **20**, 8916–8922 (2000).
11. Lo Bianco, C. *et al.* Hsp104 antagonizes alpha-synuclein aggregation and reduces dopaminergic degeneration in a rat model of Parkinson disease. *J. Clin. Invest.* **118**, 3087–3097 (2008).
12. Jackrel, M.E. *et al.* Potentiated Hsp104 variants antagonize diverse proteotoxic misfolding events. *Cell* **156**, 170–182 (2014).
13. Cushman-Nick, M., Bonini, N.M. & Shorter, J. Hsp104 suppresses polyglutamine-induced degeneration post onset in a *drosophila* MJD/SCA3 model. *PLoS Genet.* **9**, e1003781 (2013).
14. Jackrel, M.E. & Shorter, J. Reversing deleterious protein aggregation with re-engineered protein disaggregases. *Cell Cycle* **13**, 1379–1383 (2014).
15. Rosenzweig, R. *et al.* ClpB N-terminal domain plays a regulatory role in protein disaggregation. *Proc. Natl. Acad. Sci. USA* **112**, E6872–E6881 (2015).
16. Doyle, S.M., Hoskins, J.R. & Wickner, S. DnaK chaperone-dependent disaggregation by caseinolytic peptidase B (ClpB) mutants reveals functional overlap in the N-terminal domain and nucleotide-binding domain-1 pore tyrosine. *J. Biol. Chem.* **287**, 28470–28479 (2012).
17. Kedzierska, S., Akoev, V., Barnett, M.E. & Zolkiewski, M. Structure and function of the middle domain of ClpB from *Escherichia coli*. *Biochemistry* **42**, 14242–14248 (2003).
18. Rosenzweig, R., Moradi, S., Zarrine-Afsar, A., Glover, J.R. & Kay, L.E. Unraveling the mechanism of protein disaggregation through a ClpB-DnaK interaction. *Science* **339**, 1080–1083 (2013).
19. Seyffer, F. *et al.* Hsp70 proteins bind Hsp100 regulatory M domains to activate AAA+ disaggregase at aggregate surfaces. *Nat. Struct. Mol. Biol.* **19**, 1347–1355 (2012).
20. Lee, J. *et al.* Heat shock protein (Hsp) 70 is an activator of the Hsp104 motor. *Proc. Natl. Acad. Sci. USA* **110**, 8513–8518 (2013).
21. DeSantis, M.E. *et al.* Conserved distal loop residues in the Hsp104 and ClpB middle domain contact nucleotide-binding domain 2 and enable Hsp70-dependent protein disaggregation. *J. Biol. Chem.* **289**, 848–867 (2014).
22. Mackay, R.G., Helsen, C.W., Tkach, J.M. & Glover, J.R. The C-terminal extension of *Saccharomyces cerevisiae* Hsp104 plays a role in oligomer assembly. *Biochemistry* **47**, 1918–1927 (2008).
23. Lee, S. *et al.* The structure of ClpB: a molecular chaperone that rescues proteins from an aggregated state. *Cell* **115**, 229–240 (2003).
24. Lee, S., Choi, J.M. & Tsai, F.T. Visualizing the ATPase cycle in a protein disaggregating machine: structural basis for substrate binding by ClpB. *Mol. Cell* **25**, 261–271 (2007).

25. Wendler, P. *et al.* Atypical AAA+ subunit packing creates an expanded cavity for disaggregation by the protein-remodeling factor Hsp104. *Cell* **131**, 1366–1377 (2007).
26. Carroni, M. *et al.* Head-to-tail interactions of the coiled-coil domains regulate ClpB activity and cooperation with Hsp70 in protein disaggregation. *eLife* **3**, e02481 (2014).
27. Sweeny, E.A. *et al.* The Hsp104 N-terminal domain enables disaggregase plasticity and potentiation. *Mol. Cell* **57**, 836–849 (2015).
28. Hattendorf, D.A. & Lindquist, S.L. Cooperative kinetics of both Hsp104 ATPase domains and interdomain communication revealed by AAA sensor-1 mutants. *EMBO J.* **21**, 12–21 (2002).
29. Wendler, P. *et al.* Motor mechanism for protein threading through Hsp104. *Mol. Cell* **34**, 81–92 (2009).
30. DeSantis, M.E. *et al.* Operational plasticity enables hsp104 to disaggregate diverse amyloid and nonamyloid clients. *Cell* **151**, 778–793 (2012).
31. Bösl, B., Grimminger, V. & Walter, S. Substrate binding to the molecular chaperone Hsp104 and its regulation by nucleotides. *J. Biol. Chem.* **280**, 38170–38176 (2005).
32. Tessarz, P., Mogk, A. & Bukau, B. Substrate threading through the central pore of the Hsp104 chaperone as a common mechanism for protein disaggregation and prion propagation. *Mol. Microbiol.* **68**, 87–97 (2008).
33. Lee, S., Sielaff, B., Lee, J. & Tsai, F.T. CryoEM structure of Hsp104 and its mechanistic implication for protein disaggregation. *Proc. Natl. Acad. Sci. USA* **107**, 8135–8140 (2010).
34. Parsell, D.A., Kowal, A.S. & Lindquist, S. *Saccharomyces cerevisiae* Hsp104 protein: purification and characterization of ATP-induced structural changes. *J. Biol. Chem.* **269**, 4480–4487 (1994).
35. Aguado, A., Fernández-Higuero, J.A., Cabrera, Y., Moro, F. & Muga, A. ClpB dynamics is driven by its ATPase cycle and regulated by the DnaK system and substrate proteins. *Biochem. J.* **466**, 561–570 (2015).
36. Werbeck, N.D., Schlee, S. & Reinstein, J. Coupling and dynamics of subunits in the hexameric AAA+ chaperone ClpB. *J. Mol. Biol.* **378**, 178–190 (2008).
37. Mogk, A. *et al.* Roles of individual domains and conserved motifs of the AAA+ chaperone ClpB in oligomerization, ATP hydrolysis, and chaperone activity. *J. Biol. Chem.* **278**, 17615–17624 (2003).
38. Abbas-Terki, T., Donzé, O., Briand, P.A. & Picard, D. Hsp104 interacts with Hsp90 cochaperones in respiring yeast. *Mol. Cell. Biol.* **21**, 7569–7575 (2001).
39. Dulle, J.E., Stein, K.C. & True, H.L. Regulation of the Hsp104 middle domain activity is critical for yeast prion propagation. *PLoS One* **9**, e87521 (2014).
40. Oguchi, Y. *et al.* A tightly regulated molecular toggle controls AAA+ disaggregase. *Nat. Struct. Mol. Biol.* **19**, 1338–1346 (2012).
41. Schlieker, C. *et al.* Substrate recognition by the AAA+ chaperone ClpB. *Nat. Struct. Mol. Biol.* **11**, 607–615 (2004).
42. Hinnerwisch, J., Fenton, W.A., Furtak, K.J., Farr, G.W. & Horwich, A.L. Loops in the central channel of ClpA chaperone mediate protein binding, unfolding, and translocation. *Cell* **121**, 1029–1041 (2005).
43. Glynn, S.E., Martin, A., Nager, A.R., Baker, T.A. & Sauer, R.T. Structures of asymmetric ClpX hexamers reveal nucleotide-dependent motions in a AAA+ protein-unfolding machine. *Cell* **139**, 744–756 (2009).
44. Li, T. *et al. Escherichia coli* ClpB is a non-processive polypeptide translocase. *Biochem. J.* **470**, 39–52 (2015).
45. Aubin-Tam, M.E., Olivares, A.O., Sauer, R.T., Baker, T.A. & Lang, M.J. Single-molecule protein unfolding and translocation by an ATP-fueled proteolytic machine. *Cell* **145**, 257–267 (2011).
46. Maillard, R.A. *et al.* ClpX(P) generates mechanical force to unfold and translocate its protein substrates. *Cell* **145**, 459–469 (2011).
47. Olivares, A.O., Nager, A.R., Iosefson, O., Sauer, R.T. & Baker, T.A. Mechanochemical basis of protein degradation by a double-ring AAA+ machine. *Nat. Struct. Mol. Biol.* **21**, 871–875 (2014).
48. Guo, F., Maurizi, M.R., Esser, L. & Xia, D. Crystal structure of ClpA, an Hsp100 chaperone and regulator of ClpAP protease. *J. Biol. Chem.* **277**, 46743–46752 (2002).
49. Alexopoulos, J.A., Guarné, A. & Ortega, J. ClpP: a structurally dynamic protease regulated by AAA+ proteins. *J. Struct. Biol.* **179**, 202–210 (2012).
50. Haslberger, T. *et al.* M domains couple the ClpB threading motor with the DnaK chaperone activity. *Mol. Cell* **25**, 247–260 (2007).
51. Blok, N.B. *et al.* Unique double-ring structure of the peroxisomal Pex1/Pex6 ATPase complex revealed by cryo-electron microscopy. *Proc. Natl. Acad. Sci. USA* **112**, E4017–E4025 (2015).
52. Zhao, M. *et al.* Mechanistic insights into the recycling machine of the SNARE complex. *Nature* **518**, 61–67 (2015).
53. Lin, J. & Lucius, A.L. Examination of ClpB quaternary structure and linkage to nucleotide binding. *Biochemistry* **55**, 1758–1771 (2016).

ONLINE METHODS

Protein purification, ATPase and luciferase reactivation assays. WT Hsp104 was purified as previously described[12]. Hexameric Hsp104 (0.042 μM) was incubated with ATP (1 mM) at 25 °C, and the release of inorganic phosphate was monitored over 5 min with a malachite green kit (Innova). ATPase turnover was measured at a maximum rate of ~11 min^{-1}, which corresponded to a functional, ATPase-active complex. Disaggregase function was measured with luciferase reactivation assays, as previously described[30]. Aggregated luciferase (50 nM) was incubated with Hsp104 (0.167 μM hexamer) in the presence of equimolar Hsc70 and Hdj2 (Enzo Life Sciences) plus ATP (5.1 mM) and an ATP-regeneration system (1 mM creatine phosphate and 0.25 μM creatine kinase) for 90 min at 25 °C.

Cryo-sample preparation and data collection. WT Hsp104 (8.5 mg/mL) was incubated with AMP-PNP (5 mM) for 20 min at 25 °C. Samples were diluted to 0.7 mg/ml in 40 mM HEPES, pH 7.5, 40 mM NaCl, 10 mM $MgCl_2$, 1 mM DTT and 5 mM AMP-PNP, and 3.5 μl was applied to plasma-cleaned C-Flat 2/2 holey carbon grids (Protochips). Vitrification was performed with a Vitrobot (FEI), and samples were blotted for 1.5–2 s before being plunge frozen in liquid ethane. Notably, during initial attempts at imaging, Hsp104 routinely dissociated into monomers, and substantial optimization of buffer conditions, sample concentration and freezing conditions was necessary to achieve proper ice thickness and a homogeneous spread of hexameric particles. Furthermore, the use of DDM detergent was tested to increase the angular distribution, but it resulted in dissociation of the hexamer at a variety of concentrations (data not shown).

Samples were imaged with a Titan Krios TEM (FEI) operated at 300 kV. Images were recorded on a Gatan K2 Summit direct electron detector operated in counted mode at 50,000× nominal magnification calibrated to 1.00 Å/pixel. Dose-fractionated imaging was performed through semiautomated collection methods with UCSF Image 4 (ref. 54) with a defocus range of 1.5–3 μm. The total exposure time was 8 s with 0.2-s frames, with a cumulative dose of ~45 $e^{-}/Å^2$ for 40 frames. Motion-corrected frames were summed, excluding the first two frames, and the FFT was visually inspected for sufficient Thon rings before additional processing[55].

Image processing and 3D refinement. All micrographs were CTF-corrected with CTFFIND4 (ref. 56), and poorly corrected micrographs were removed after visual inspection of the FFT and CTF estimation. An initial single-particle data set was achieved by manual particle picking with e2boxer (EMAN2)[57], which yielded ~50,000 particles from 1,731 micrographs. Well-populated reference-free 2D class averages, determined with Relion[58], were used for templated automated particle picking with the Template Picker in Appion[59], and a data set of ~200,000 single particles from 1,930 micrographs was generated. The total data set of ~250,000 particles was initially sorted after 2D classification by removal of particle images from poorly resolved class averages, thus resulting in a total data set of ~190,000 particles. All subsequent 3D processing was performed with Relion[7] with no symmetry imposed, on the basis of the asymmetric arrangement identified in the 2D class averages (**Fig. 1b**). A previously determined cryo-EM 3D reconstruction of ATP–Hsp104 (EMD-1600)[29], low-pass-filtered to 50 Å, served as an initial model for 3D classification and refinement. The eight models generated from 3D classification appeared homogenous (data not shown); therefore, the full data set was used for initial gold-standard 3D refinement. The resulting 3D model refined to an estimated resolution of 7.5 Å (data not shown). Z-score parameters based on this refinement, defined in Relion, were written for the data set, and the data set was trimmed to the highest Z score for 160,000 particles. Additional 3D refinement performed with this trimmed data set resulted in a final model with an estimated resolution of 6.54 Å with the 0.143 FSC criterion (**Supplementary Fig. 1e**). Additional trimming based on the Z score produced no improvement, and extensive 3D classification and refinement of individual classes as well as local refinement with 3D masking was tested and did not yield improvements in the map. Thus, the resolution is probably limited by the flexibility of multiple regions in the complex (**Supplementary Fig.1h**) and moderate preferred orientation (**Supplementary Fig. 1f**). For the final sharpened map, the postprocessing procedure was used to generate a soft mask for the two half maps before FSC estimation, which was determined to be 5.64 Å (**Supplementary Fig. 1e**). Automated B-factor sharpening was performed on the combined map with an estimated −188 B factor. The local resolution was estimated with ResMap on the unsharpened map[60].

Modeling. This final sharpened map was used for all rigid-body docking and flexible fitting of atomic structures. Rigid-body fitting was performed with UCSF Chimera[61]. Initial comparisons were performed by fitting individual protomers with the protomers in the *T. thermophilus* ClpB crystal structure (PDB 1QVR) but resulted in a low cross-correlation value, and clear conformational differences were apparent. Individual subdomains (NTD, NBD1 large, NBD1 small, MD (residues 409–467), NBD2 large and NBD2 small) from the crystal structure were then docked as rigid bodies, thus resulting in an improved fit; however, a number of AAA-domain helices did not align with the density. Therefore, to more accurately interrupt the map, a homology model of Hsp104 (residues 6–857) was determined from the ClpB structure (residues 4–850) with SWISS_MODEL[62], and this was followed by rigid-body docking of the subdomains. Flexible fitting of the protomer subvolumes and the entire hexamer map was then performed with phenix.real_space_refine[63] with backbone carbons of our homology model. The real-space refinement was implemented at 6σ, 6-Å resolution, and the cross-correlation was improved from 0.72 to 0.9 for the complete map after refinement. To visualize the presence of density in the nucleotide pockets, difference maps were generated by subtracting a simulated density map of the Hsp104 homology model without AMP-PNP from the final refined map, and are shown at 5σ (**Supplementary Fig. 2b**). From the difference map, clear density was observed at nine sites, and partial density was observed at two sites; therefore, AMP-PNP was included in the model at these sites and docked on the basis of the ClpB structure. Modeling of the P2–P4 NTDs was facilitated by localization of the well-defined NTD–NBD1 connecting density as well as regions that could be attributed to the larger A1 and A6 helices that make up the hydrophobic substrate–binding cleft[15]. Manual modeling of the tyrosine loop regions was performed in COOT[64]. Loop regions within the NBD1 domain (248–260 and 287–300) were modeled by backbone positioning within the density; residues 251–259 and 292–297 could not be modeled in the density. Notably, a major shift was required to model the NBD2 tyrosine loop (656–669), which showed a distinct curve away from the flanking helices. Similarly, the most central portion of the loop lacked density and was not modeled (659–666). All images were generated with UCSF Chimera[61].

54. Li, X., Zheng, S., Agard, D.A. & Cheng, Y. Asynchronous data acquisition and on-the-fly analysis of dose fractionated cryoEM images by UCSFImage. *J. Struct. Biol.* **192**, 174–178 (2015).
55. Li, X. *et al.* Electron counting and beam-induced motion correction enable near-atomic-resolution single-particle cryo-EM. *Nat. Methods* **10**, 584–590 (2013).
56. Rohou, A. & Grigorieff, N. CTFFIND4: fast and accurate defocus estimation from electron micrographs. *J. Struct. Biol.* **192**, 216–221 (2015).
57. Tang, G. *et al.* EMAN2: an extensible image processing suite for electron microscopy. *J. Struct. Biol.* **157**, 38–46 (2007).
58. Scheres, S.H. RELION: implementation of a Bayesian approach to cryo-EM structure determination. *J. Struct. Biol.* **180**, 519–530 (2012).
59. Lander, G.C. *et al.* Appion: an integrated, database-driven pipeline to facilitate EM image processing. *J. Struct. Biol.* **166**, 95–102 (2009).
60. Kucukelbir, A., Sigworth, F.J. & Tagare, H.D. Quantifying the local resolution of cryo-EM density maps. *Nat. Methods* **11**, 63–65 (2014).
61. Pettersen, E.F. *et al.* UCSF Chimera: a visualization system for exploratory research and analysis. *J. Comput. Chem.* **25**, 1605–1612 (2004).
62. Biasini, M. *et al.* SWISS-MODEL: modelling protein tertiary and quaternary structure using evolutionary information. *Nucleic Acids Res.* **42**, W252–W258 (2014).
63. Afonine, P.V. *et al.* Towards automated crystallographic structure refinement with phenix.refine. *Acta Crystallogr. D Biol. Crystallogr.* **68**, 352–367 (2012).
64. Emsley, P., Lohkamp, B., Scott, W.G. & Cowtan, K. Features and development of Coot. *Acta Crystallogr. D Biol. Crystallogr.* **66**, 486–501 (2010).

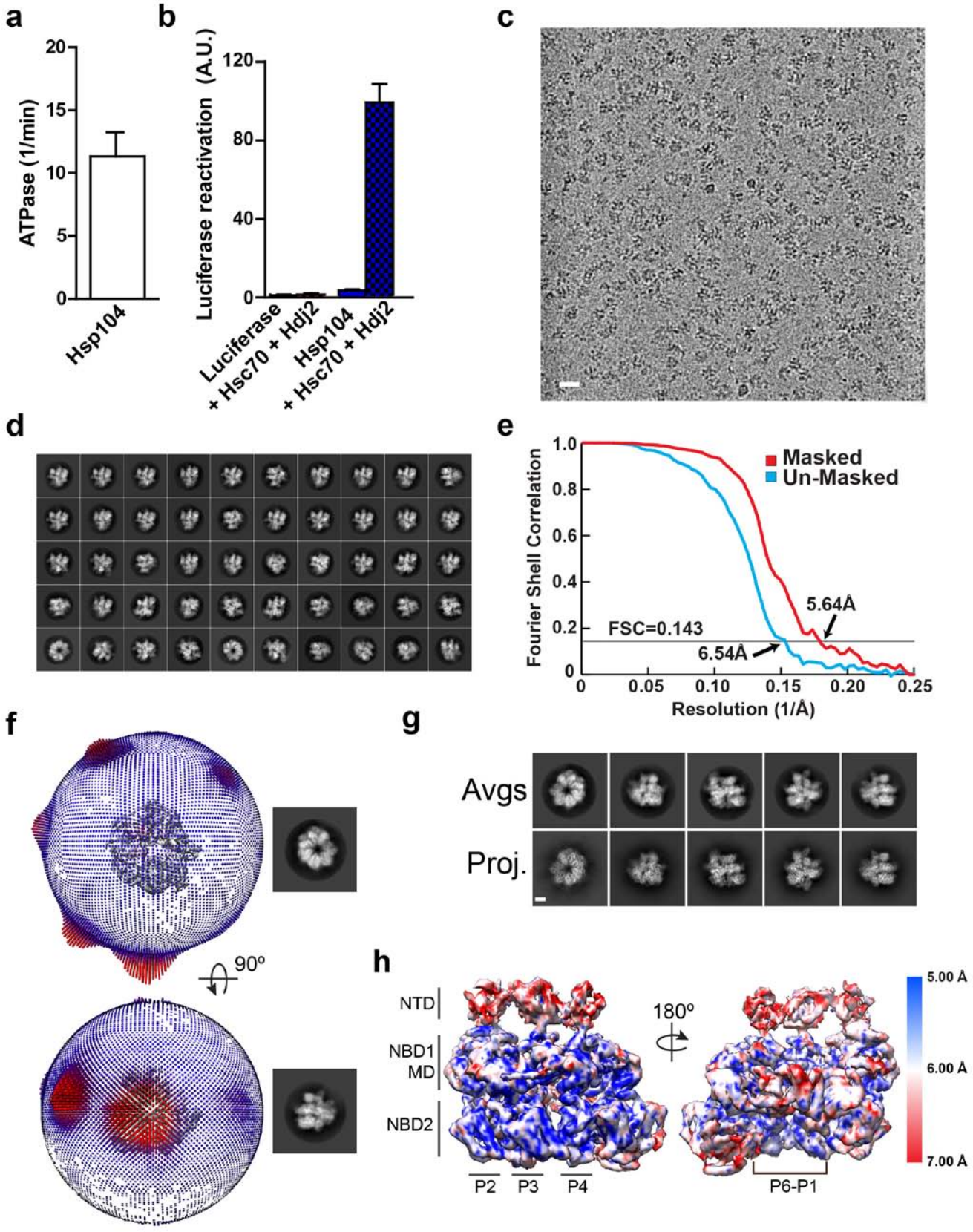
a
ATPase (1/min)
20
15
10
5
0
Hsp104
b
Luciferase reactivation (A.U.)
120
80
40
0
Luciferase
+ Hsc70 + Hdj2
Hsp104
+ Hsc70 + Hdj2
c
d
e
Fourier Shell Correlation
1.0
0.8
0.6
0.4
0.2
0
Masked
Un-Masked
5.64Å
FSC=0.143
6.54Å
0
0.05
0.10
0.15
0.20
0.25
Resolution (1/Å)
f
90°
g
Avgs
Proj.
h
NTD
NBD1
MD
NBD2
180°
5.00 Å
6.00 Å
7.00 Å
P2
P3
P4
P6-P1

Supplementary Figure 1

Functional and cryo-EM analysis of Hsp104.

(a) Purified Hsp104 hexamer is active for ATPase function, measured as the release of inorganic phosphate over 5 minutes. Value represents mean ± SEM (n = 3). (b) Purified Hsp104 is active for luciferase disaggregation. Recovered luciferase luminescence determined following incubations with Hsp104 plus (checkered bars) or minus (clear bars) equimolar Hsc70 and Hdj2. Values represent means ± SEM (n = 3). (c) Representative cryo-EM micrograph of Hsp104 hexamers. Scale bar equals 200 Å (d) 2D reference free class averages of Hsp104. The top 50 populated views are shown. (e) Gold standard FSC curve for the un-masked and masked reconstructions of the final model estimated from the FSC=0.143 criterion to be 6.54 Å and 5.64 Å, respectively. (f) 3D plot of the angular distribution for the particles that contributed to the final model. Top and side view orientations are shown with the corresponding 2D projection average. (g) Comparison of reference free class averages and 2D projections of the final 3D reconstruction. Scale bar equals 50 Å. (h) Local resolution of the 3D reconstruction determined by ResMap[1] and shown from 5 Å (blue) to 7 Å (red).

1 Kucukelbir, A., Sigworth, F. J. & Tagare, H. D. Quantifying the local resolution of cryo-EM density maps. *Nat Methods* **11**, 63-65, doi:10.1038/nmeth.2727 (2014).

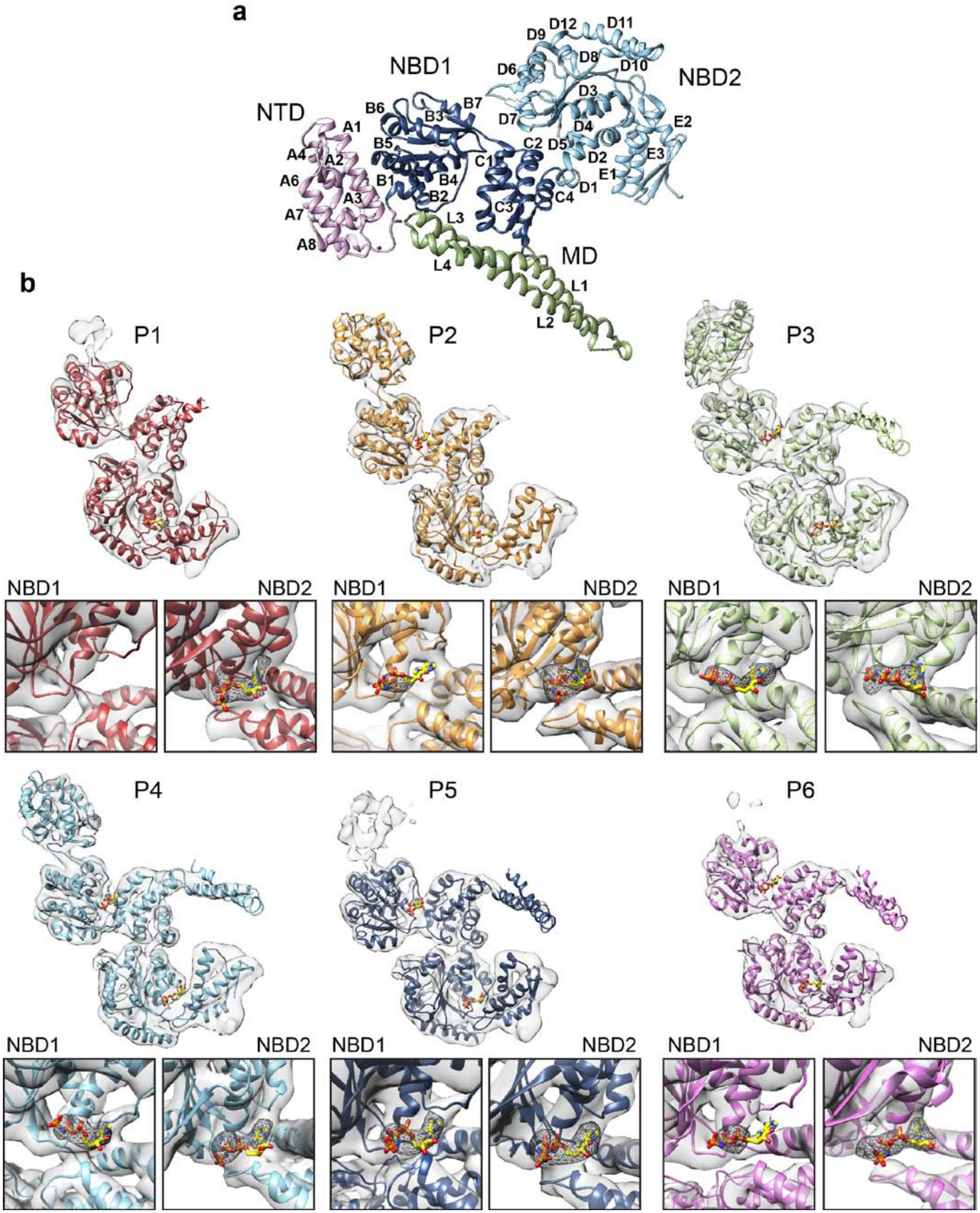
a
NBD1
NBD2
NTD
MD
D9
D12
D11
D8
D6
D10
D3
B6
B7
B3
D7
D4
E2
A1
B5
C2
D5
D2
E3
A4
A2
C1
E1
A6
B1
B4
D1
A3
B2
C4
A7
C3
L3
A8
L4
L1
L2
b
P1
P2
P3
NBD1
NBD2
NBD1
NBD2
NBD1
NBD2
P4
P5
P6
NBD1
NBD2
NBD1
NBD2
NBD1
NBD2

Supplementary Figure 2

ClpB structure and molecular models of the Hsp104 protomers.

(a) ClpB structure labeled for reference, as previously reported[1] (PDB: 1QVR), with helices indicated for the NTD (A), NBD1 large (B) and small (C) subdomains, MD (L) and NBD2 large (D) and small (E) subdomains. (b) Hsp104 molecular models for each protomer in the asymmetric hexamer with the segmented density shown at 5σ. Below are enlarged views of the nucleotide pockets with difference maps, generated by subtracting a model with no nucleotide from the cryo-EM map, shown as mesh to visualize density for bound nucleotide. AMPPNP is shown as sticks where density is observed in the pocket for the difference maps.

1 Lee, S. *et al.* The structure of ClpB: a molecular chaperone that rescues proteins from an aggregated state. *Cell* **115**, 229-240 (2003).

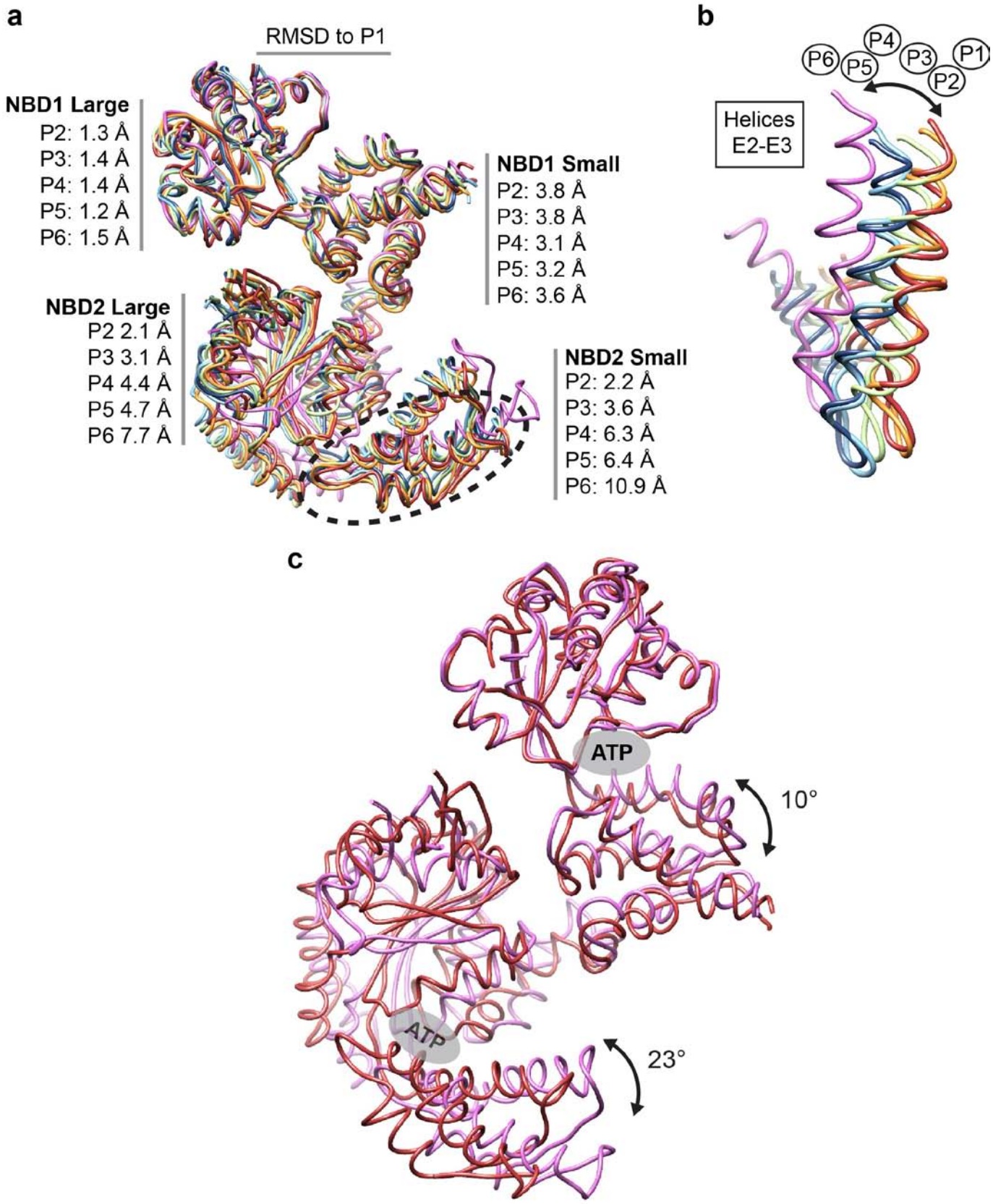
a
RMSD to P1
NBD1 Large
P2: 1.3 Å
P3: 1.4 Å
P4: 1.4 Å
P5: 1.2 Å
P6: 1.5 Å
NBD1 Small
P2: 3.8 Å
P3: 3.8 Å
P4: 3.1 Å
P5: 3.2 Å
P6: 3.6 Å
NBD2 Large
P2 2.1 Å
P3 3.1 Å
P4 4.4 Å
P5 4.7 Å
P6 7.7 Å
NBD2 Small
P2: 2.2 Å
P3: 3.6 Å
P4: 6.3 Å
P5: 6.4 Å
P6: 10.9 Å
b
P6
P5
P4
P3
P2
P1
Helices
E2-E3
c
ATP
10°
ATP
23°

Supplementary Figure 3

Conformational differences in the AAA+ domains of the individual protomers.

(a) Overlay of the backbone trace for the protomer NBDs following alignment to the P1 NBD1 large subdomain. RMSD values compared to P1 are shown and identify increasing differences from P2 to P6. (b) Enlarged view of circled region of (a) showing helices E2 and E3 for the 6 aligned protomers, highlighting conformational changes for P1 to P6. (c) Overlay of P1 and P6 protomers that interact at the hexamer interface, showing conformational changes including rotation of the NBD1 and NBD2 small subdomains.

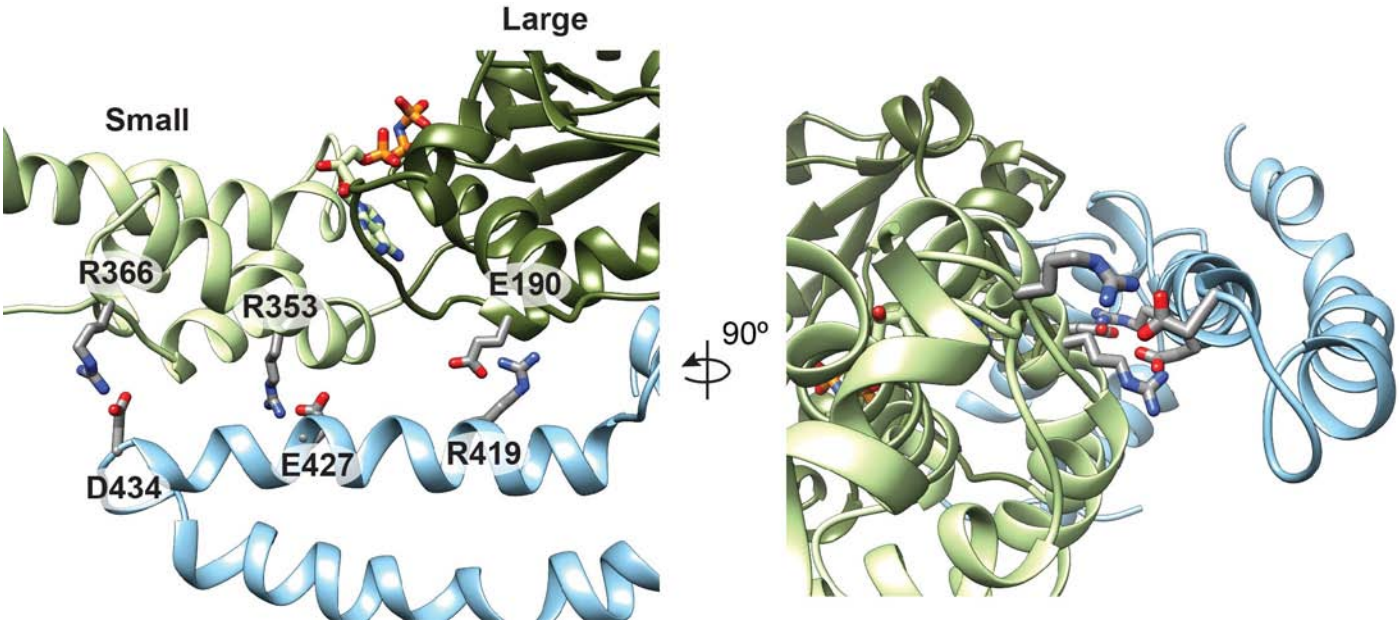

Supplementary Figure 4

Proposed MD NBD1 cross-protomer stabilizing interactions.

Views showing model with proposed salt bridge interactions between MD-L1 and adjacent NBD1 that bridge the large and small AAA+ subdomains across nucleotide-binding pocket.

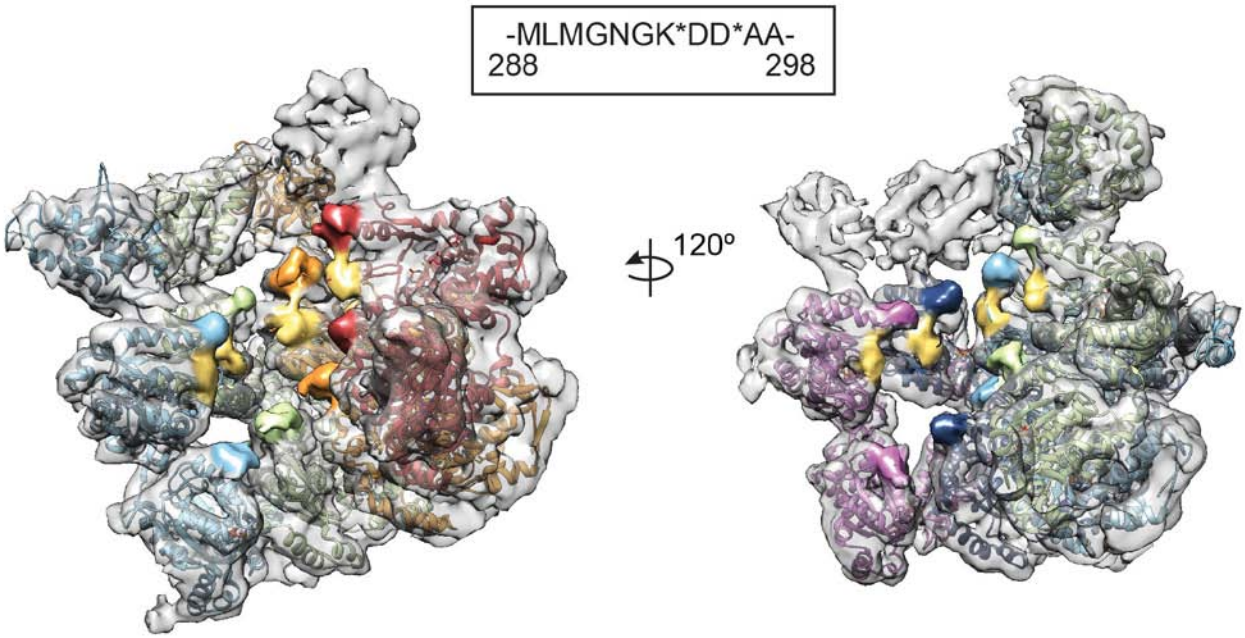

Supplementary Figure 5

Additional NBD1 pore loops line the Hsp104 channel and potentially function as substrate-binding sites.

(a) Views of the channel interface with density corresponding to putative NBD1 substrate binding surfaces shown in yellow that include flexible pore loop residues 288-298. Adjacent Tyr pore loop regions are shown as in Figure 5. Hsp104 sequence is shown with conserved charged residues indicated (asterisk).